

Fabrication of TiO₂ Binary Inverse Opals without Overlayers via the Sandwich-Vacuum Infiltration of Precursor

Zhongyu Cai,[†] Jinghua Teng,[‡] Zhigang Xiong,[†] Yanqiang Li,^{||} Qin Li,[§] Xianmao Lu,[†] and X. S. Zhao^{*,†}

[†]Department of Chemical and Biomolecular Engineering, National University of Singapore, 4 Engineering Drive 4, Singapore 117576

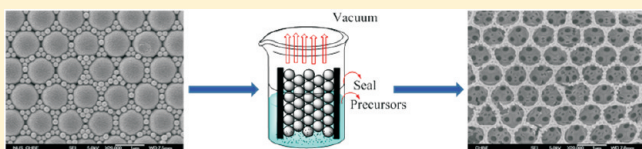
[‡]Institute of Materials Research and Engineering, Agency for Science, Technology and Research (A*STAR), 3 Research Link, Singapore 117602

^{||}Institute of Multifunctional Materials (IMM), Laboratory of New Fiber Materials and Modern Textile, College of Chemistry, Chemical Engineering and Environment, Qingdao University, Qingdao 266071, PR China

[§]Department of Chemical Engineering, Curtin University, GPO Box U1987, Perth WA 6845, Australia

 Supporting Information

ABSTRACT: A sandwich-vacuum method was demonstrated for the fabrication of titania (TiO₂) binary inverse opals with an open surface. In this method, a moisture-stable TiO₂ precursor was backfilled into the interstitial spaces of polystyrene binary colloidal crystals (PS bCCs), which served as a template. Removal of the template by calcination yielded TiO₂ binary inverse opals with a 3D-ordered macroporous (3DOM) structure. Optical reflectance spectra revealed the existence of a pseudostop band gap in the 3DOM TiO₂ samples. The position of the pseudostop band gap shifted to the low-wavelength region as the number ratio of small over large PS spheres was increased in the template. The sandwich-vacuum method proved to be simple and rapid for the fabrication of TiO₂ binary inverse opals without overlayers in large domains. The 3DOM TiO₂ materials were used as a photocatalyst for the degradation of benzoic acid. Results showed that in comparison to TiO₂ nanoparticles prepared under the same sintering conditions, the 3DOM TiO₂ materials displayed enhanced photocatalytic activity.



INTRODUCTION

Inverse opals, or 3D-ordered macroporous (3DOM) materials, have attracted considerable interest in recent years owing to their distinct structural features. Through replicating a typical face-centered cubic (fcc) opaline template, inverse opals with high interconnected porosity, extremely uniform size, and periodic distributions of pores can be fabricated. These structural features are important to the design of photonic crystals,^{1–4} sensors,^{5,6} power sources,^{7,8} catalysts,^{4,9–11} and various other applications. The most frequently used method of preparing such ordered structures is based on colloidal crystal templating, which typically requires three sequential steps. First, a colloidal crystal template is fabricated by using monodisperse latex or silica microspheres; then a matrix phase or a precursor is infiltrated or deposited into the interstices of the template; finally, the template is selectively removed and an inverse porous structure is formed.^{10,12–15} Using this method, inverse opals of various metal oxides, such as titania (TiO₂), zirconia (ZrO₂), tantalum oxide (Ta₂O₅), and niobium oxide (NbO₂), have been prepared.^{10,12–17}

Among various inverse opals, 3DOM TiO₂ has gained particular attention because of its novel optical and electronic properties, high specific surface area, and a wide variety of applications in photocatalysis^{18,19} and solar cells.^{20–24} Conventionally, 3DOM TiO₂ was fabricated directly by using titanium alkoxides as the sol–gel precursor for the infiltration of synthetic opals.^{10,25} However, there are difficulties associated with forming ordered

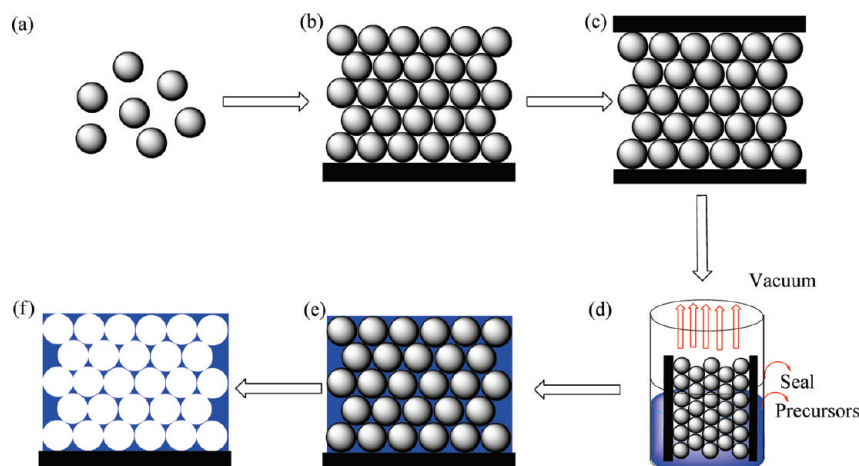
TiO₂ inverse opals using this method that can be attributed to two reasons. First, titanium alkoxides are air- and moisture-sensitive; therefore, it is hard to control the degree of infiltration.^{10,16} The other reason is that the excess precursor can form overlayers on top of the 3DOM structure.²⁶ To address these two challenges, various approaches have been developed. For example, diluting the precursor in ethanol can lower the viscosity and improve the wetting properties of the sol precursor. However, these approaches typically require multiple infiltration steps in order to achieve a mechanically robust structure.^{27,28}

Holland et al.¹⁰ described a vacuum filtration method to fabricate TiO₂, ZrO₂, and alumina (Al₂O₃) inverse opals by using latex template. Despite its success in the fabrication of ZrO₂ and Al₂O₃ inverse opals, the precursor for TiO₂ prehydrolyzes before filtration^{15,29} when exposed to the atmosphere. Very recently, an elegant method was developed by Bartl et al.²⁶ to solve this problem. A highly air- and moisture-stable sol–gel precursor solution was used to infiltrate the interstitial spaces of a polystyrene (PS) template. Subsequently, a novel “lift-off/turnover” strategy was employed to reduce the overlayer on top of the 3DOM structure. Finally, TiO₂ inverse opals with open pores were obtained via calcination. However, this method involves multiple steps, and the

Received: January 10, 2011

Revised: February 28, 2011

Published: March 17, 2011

Scheme 1. Fabrication Process of TiO₂ Inverse Opals without Overlayers

formation of overlayers cannot be completely avoided. In a very recent study, Zou et al.¹⁶ reported a forced impregnation approach to the fabrication of 3DOM metal oxides. Through this simple and versatile approach, large-area 3DOM structures of TiO₂, Nb₂O₅, Ta₂O₅, and ZrO₂ with high porosity were prepared. Unfortunately, this approach cannot avoid the formation of an overlayer either.

Here we report a sandwich-vacuum method for the infiltration of a modified precursor into the interstitial spaces of PS binary colloidal crystals (bCCs) to form TiO₂ binary inverse opals without any overlayer. Before infiltration, titanium alkoxide was treated with trifluoroacetic acid and hydrochloric acid. This modification yielded a highly air- and moisture-stable sol–gel precursor solution by slowing down the kinetics of condensation.^{26,30–32} In addition, the use of trifluoroacetic acid increased the precursor hydrophobicity, which facilitated the infiltration process.²⁶ After heat treatment of the PS bCCs, a glass cover slide was placed on top of the samples and clamped with two clips. Subsequently, a vacuum pump was utilized to remove the air trapped in the interstitial spaces of the PS bCCs. The voids were then filled with the TiO₂ precursor as a result of the pressure difference and capillary force. Finally, the bCC template was selectively removed by calcination. This simple method was proven to be effective in fabricating high-quality TiO₂ binary inverse opals without overlayers. We further studied photodegradation using the TiO₂ binary inverse opals as catalysts and observed enhanced photocatalytic performance.

EXPERIMENTAL SECTION

Materials. All chemicals, including styrene (99%, Aldrich), potassium persulfate (99%, Aldrich), ethanol (99.95%, Aldrich), sulfuric acid (98%, Merck), hydrogen peroxide (35%, Scharlau Chemie S.A.), titanium(IV) isopropoxide (97%, Sigma-Aldrich), benzoic acid (95%, BDH Chemicals), hydrochloric acid (37%, Sigma-Aldrich), and trifluoroacetic acid (99%, Sigma-Aldrich), were used as received.

Fabrication of TiO₂ Binary Inverse Opals. The fabrication of TiO₂ binary inverse opals was conducted in six sequential steps: (i) synthesis of PS microspheres, (ii) fabrication of PS bCCs, (iii) heat treatment, (iv) sandwich binding between two substrates with clips, (v) infiltration of precursors, and (vi) drying and calcinations (Scheme 1). The detailed procedures are described below.

Table 1. Recipe for the Fabrication of Binary PS Colloidal Crystals

sample	$N_{S/L}$	PS (1000 nm) 8.70% (μL)	PS (170 nm) 1.54% (μL)	volume fraction ratio ($V_{S/L}$)
PS bCCs (2)	2	2000	110.8	19.78
PS bCCs (4)	4	2000	221.7	9.89
PS bCCs (8)	8	2000	443.4	4.95

PS microspheres with diameters of 170 and 1000 nm were synthesized using an emulsifier-free emulsion polymerization method.³³ PS bCCs were fabricated following the horizontal deposition method previously developed in our laboratory.³⁴ Typically, microscope cover glasses (22 mm \times 22 mm \times 0.3 mm, Deckgläser) were used as substrates for the deposition of bCCs. The silica substrates were treated in piranha solution (3:1 v/v 98% H₂SO₄/35% H₂O₂) at 60 °C for 2 h before use. A mixed colloidal suspension (60 μL ; an 8.70 vol % solution for the large microspheres and a 1.54 vol % solution for the small microspheres) was then drop cast on the substrate to spread over the whole surface. Three compositions of PS bCCs were fabricated by varying the ratio of small to large microspheres in the mixed colloidal suspension (details in Table 1).

The TiO₂ precursor was prepared by adding 4 mL of titanium isopropoxide to a mixture of 3.2 mL of trifluoroacetic acid and 0.8 mL of hydrochloric acid under vigorously stirring. After 30 min, a certain volume of absolute ethanol was added to the mixture to adjust the viscosity of the solution. The whole process was handled in a fume hood. Before infiltration with the TiO₂ precursor solution, the PS bCCs were annealed at 105 °C for 20 min. A sandwich-vacuum technique was employed for the infiltration. Typically, the PS bCC template was covered with a smooth glass slide and pressed together with two clips. The close contact between the bCC template and the glass slide may avoid the formation of a TiO₂ overlayer. Then half of the template was immersed in the modified TiO₂ precursor solution, and the other half was exposed to air. The container holding the TiO₂ precursor solution was sealed with a stopper and connected to a vacuum pump. Under vacuum, the interstitial spaces of the bCC template were easily infiltrated with the TiO₂ precursor because of the pressure difference and capillary force. After infiltration, the opal/TiO₂ composite was allowed to dry for 24 h in air. Then, the resultant samples were calcinated at 500 °C (1 °C/min) for 4 h to remove the template, eventually forming anatase TiO₂ binary inverse opals. At the same sintering temperature as that of TiO₂ binary

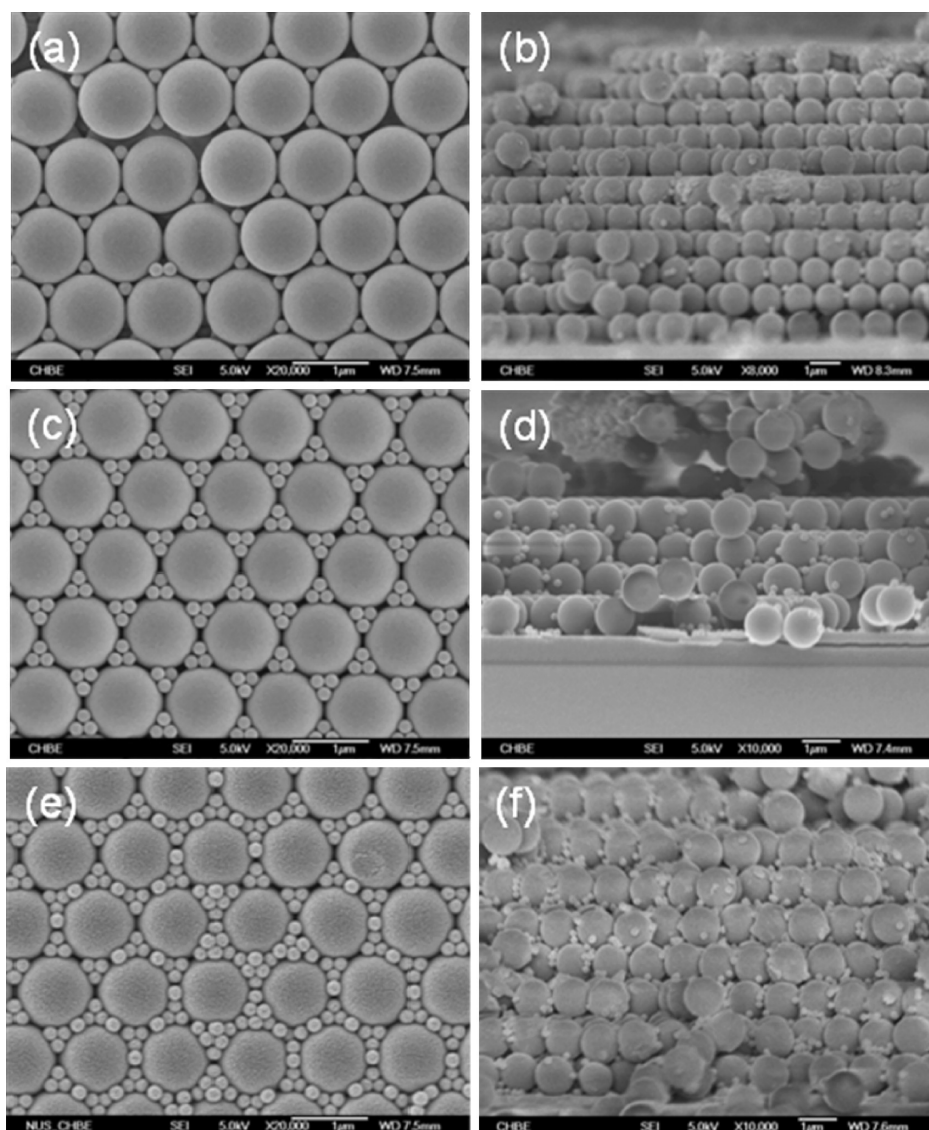


Figure 1. PS binary opals fabricated by using 170 and 1000 nm PS microspheres. The number ratios of small (170 nm) to large (1000 nm) microspheres are (a) 2, (c) 4, and (e) 8, respectively. (b, d, f) Cross-sectional views of PS bccs corresponding to the samples in a, c, and e, respectively.

inverse opals, TiO_2 nanoparticles were prepared by using the same modified TiO_2 precursor.

Characterization. The scanning electron microscope (SEM) images of the PS bccs and TiO_2 binary inverse opals were recorded by using a JEOL JSM-6700F field-emission SEM (FESEM). A field-emission transmission electron microscope (FETEM, JEOL JEM-2100F) was applied to analyze the structure of the macroporous TiO_2 . The X-ray diffraction (XRD) patterns were acquired with a Shimadzu XRD-6000 X-ray diffractometer (LABX XRD-6000) using $\text{Cu K}\alpha$ irradiation at a scan rate of 2° min^{-1} . The optical spectra were obtained on a Shimadzu UV-3600PC UV–vis–near-IR (UV–vis–NIR) spectrophotometer. The specific surface areas of the samples were measured on an ASAP 2020 surface area and porosity analyzer (Micromeritics, USA) by the Brunauer–Emmet–Teller (BET) method.

Photocatalytic Activity. The photocatalytic activity of the TiO_2 binary inverse opals was evaluated for the degradation of benzoic acid (BA) under the irradiation of a 300 W mercury lamp with a cut-off filter ($<340 \text{ nm}$). The initial concentration of BA in the reactor is 7 ppm. Ten milligrams of the solid sample was dispersed uniformly in a 100 mL beaker containing the BA solution. Magnetic stirring was used throughout the

entire reaction period. Before the lamp was switched on, the suspension was stirred for about 30 min in the dark to ensure that the adsorption equilibrium of BA had been attained on the catalyst surface. Small aliquots were withdrawn at each given time interval and quantitatively determined using a Shimadzu-1601 PC UV–visible spectrophotometer.

RESULTS AND DISCUSSION

FESEM images of the as-prepared PS binary opals are shown in Figure 1. Three-dimensionally ordered structures were obtained using the horizontal deposition method and have been observed before.³⁴ For the PS binary opals fabricated with a number ratio of small to large microspheres of 2, most of the interstitial voids among the large microspheres are filled with one small PS microsphere (Figure 1a). When the number ratio is increased to 4, three small microspheres are embedded in the voids (Figure 1c). For a number ratio of 8, each large microsphere is surrounded by ~ 15 small microspheres (Figure 1e). Figure 1b,d,f are the cross-sectional views of the PS bccs at number ratios of 2, 4, and 8, respectively, which reveal that the

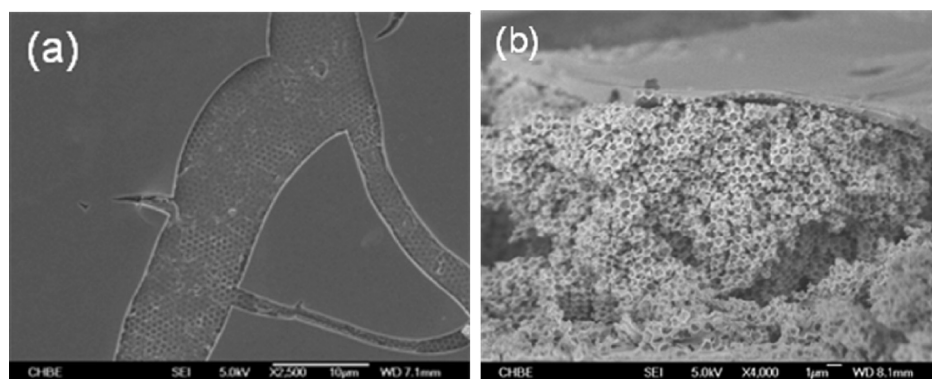


Figure 2. TiO_2 binary inverse opals fabricated by using a conventional dip-coating method. (a) Top view. (b) Cross-sectional view.

large microspheres are clearly in the form of an fcc lattice. However, the small microspheres inside are not as ordered as those on the top surface. They are evenly distributed over the surface of the large microspheres.

The PS bCCs were then subjected to heat treatment followed by infiltration of the titanium precursor. After the selective removal of the PS microspheres via calcination, large-area TiO_2 binary inverse opals were obtained. We first employed a conventional infiltration method (dip-coating method) to form TiO_2 binary inverse opals. The top and cross-sectional views of the resultant structure show that there are no interconnected open pores but a smooth surface with cracks was formed (Figure 2). An overlayer was formed on top of the TiO_2 binary inverse opals (Figure 2b), indicating that excess precursor is inevitable in inducing the formation of overlayers by using the conventional infiltration technique.

The conventional infiltration technique is ineffective in fabricating TiO_2 binary inverse opals without overlayers. Therefore, a sandwich-vacuum technique developed in our laboratory was employed to infiltrate the interstices of the PS bCC templates with the TiO_2 precursor. Figure 3a,d,g illustrates the detailed structure of the resultant TiO_2 binary inverse opals at number ratios of small to large microspheres of 2, 4 and 8, respectively. These TiO_2 binary inverse opals exhibit highly ordered structure over large domains ($>10\ \mu\text{m} \times 10\ \mu\text{m}$) with few defects. The formation of overlayers was eliminated completely. High-magnification SEM images (Figure 3b,e,h) reveal two sets of pore structures with defined sizes of ~ 670 and ~ 115 nm, respectively. In addition, an increase in the number ratio of small PS microspheres led to 3DOM TiO_2 structures with higher porosity. The pores were formed at the sites originally taken by the large and small PS microspheres, and the three large windows were the contact points of large PS microspheres. For all of the binary inverse opals, the average diameter of the macropores is ~ 670 nm, indicating an $\sim 33\%$ contraction of the TiO_2 binary inverse opals. This shrinkage may be caused by both the melting of the PS microspheres and the sintering of the produced powders. The smallest randomly distributed windows were formed at the touch points of the small microspheres with the large ones. The ordered large windows and random small windows indicate that the large PS microspheres were packed in fcc form but the small ones were not packed in a highly ordered fashion inside the colloidal crystals. By examining the distribution of the large and small windows presented in the cross-sectional images (Figure 3c,f), it can be inferred that the general distribution of the small microspheres in the bCCs appears to be uniform. However, inside the bCCs, the

arrangement of the small microspheres in the interstitial spaces among the large microspheres is not as highly ordered as those on the top layer. Figure 3f also demonstrates an ordered structure along the $\langle 100 \rangle$ direction with 12 layers of pores. The cross-sectional image of 3DOM TiO_2 at a lower magnification (Figure 3i) shows that TiO_2 binary inverse opals over relatively large areas can be obtained via this method. An uneven distribution of the small microspheres in the bCCs was also revealed from the cross-sectional views. As shown in Figure 3c,f,i, the concentration of small windows slightly increases toward the upper layers, indicating the increasing number of microspheres in the upper layers.

The major advantage of this fabrication method for TiO_2 binary inverse opals is the complete elimination of the overlayers, which can be attributed to the combination of the following two factors: (1) the use of a trifluoroacetic acid-modified precursor and (2) the application of the sandwich-vacuum technique. Using a trifluoroacetic acid-modified precursor may result in uniform wetting of the PS template because the solubilized titanium oxide together with trifluoroacetic acid molecules can form stable hydrophobic building blocks for further cross-linking.³² The use of the sandwich-vacuum method avoids the formation of bulk layers on top of the TiO_2 films. This is the major advantage of this method over other methods. Although the methods developed by Bartl et al.²⁶ and Zou et al.¹⁶ may prevent the fast hydrolysis of the TiO_2 precursor, complicated procedures are needed²⁶ and the overlayers cannot be completely avoided.^{16,26}

Figure 4 displays the TEM images of the TiO_2 binary inverse opals. Figure 4a illustrates the ordered 3DOM structure of the TiO_2 binary inverse opals, and Figure 4b–d shows top views of TiO_2 inverse opals at higher magnifications. These images clearly indicate the spatial periodicity of the closely packed macropores. The average pore thickness of the wall shown in Figure 4b–d is ~ 50 nm, thus it is mechanically robust enough to maintain the integrity of the 3DOM structure. Most of the ordered structures remained intact even under ultrasonication during TEM sample preparation (Figure 4a). The number of small windows increased with the increase in the number ratio of small to large microspheres (Figure 4b–d). However, the number of windows was less than the theoretical values in these three samples, indicating an uneven distribution of small microspheres inside the bCC templates. This result is consistent with the FESEM results shown in Figure 3. It should be noted that, in comparison with the fabrication of TiO_2 unary inverse opals, the fabrication of TiO_2 binary inverse opals is more complicated, with a number of interactions combining with smaller interstices to be filled. The

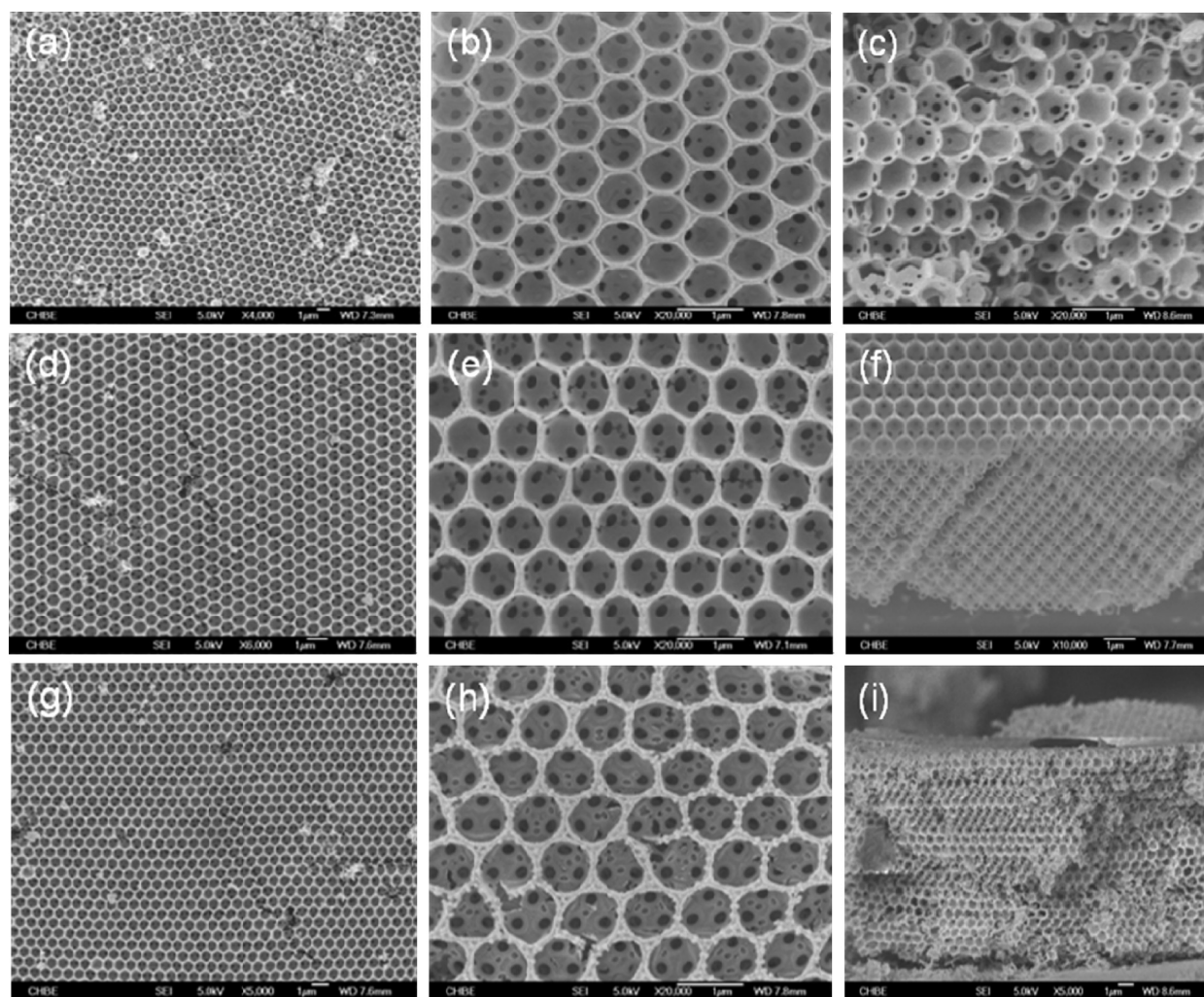


Figure 3. Top and cross-sectional views of TiO_2 binary inverse opals fabricated using the sandwich-vacuum infiltration technique. The number ratios of small to large microspheres are (a–c) 2, (d–f) 4, and (g–i) 8.

highly ordered structure together with interconnected pores over a relatively large area further proves the effectiveness of this sandwich-vacuum infiltration technique. High-resolution TEM images show d spacings of 3.52 Å (Figure 4e) and 2.38 Å (Figure 4f), corresponding to the {101} and {004} planes of the TiO_2 structure, respectively.

Figure 5 shows a typical XRD pattern recorded for the TiO_2 binary inverse opals. Characteristic diffraction peaks corresponding to anatase (101), (103), (004), (112), (200), (105), and (211) reflections can be found at $2\theta = 25.28, 36.95, 37.80, 38.58, 48.05, 53.89,$ and 55.06 , respectively (JCPDS card 21-1272). The relatively sharp peaks indicate that the sample is composed of highly crystalline anatase TiO_2 .

The reflectance spectra of both PS bCCs and TiO_2 binary inverse opals were recorded. It was found that for both structures the reflectance can be influenced by the number ratio of small to large microspheres. Figure 6 shows the reflectance spectra of PS bCCs fabricated at number ratios of small to large microspheres of 2, 4 and 8, respectively. The distinctive peaks between 2300 and 2400 nm indicate the long-range ordering of the PS bCCs. The slight red shift at higher number ratios is due to the increase in the effective refractive index caused by the high filling ratio of small PS microspheres in the interstitial spaces of large PS

microspheres. The pronounced ripples on the reflectance peaks of the bCCs can be treated as Fabry–Pérot fringes, which suggests that the refractive index varies among the crystal layers.³⁶ Although small microspheres may contribute to the effective refractive index, their less-ordered arrangement does not affect the optical properties significantly.

The reflectance spectra of the TiO_2 binary inverse opals are shown in Figure 7. The sharp peaks between 1200 and 1300 nm suggest that these binary inverse opals have a uniform structure. With the increase in the number ratio of small to large PS microspheres, the porosity of the resultant TiO_2 binary inverse opals increases, leading to a decrease in the effective refractive index and hence a blue shift of the reflectance peak. Therefore, the stop band positions of the TiO_2 binary inverse opals are consistent with the composition of the PS bCC templates. This interesting optical property of TiO_2 binary inverse opals may find applications in bio- or chemosensing.³⁴

Table 2 compares the theoretical and measured peak wavelengths of the PS bCCs and TiO_2 binary inverse opals. The theoretical peak wavelengths were calculated according to Bragg's equation for the absorption maxima with regard to the (111) crystal face, $\lambda_{\text{max}} = (8/3)^{1/2} D (n_{\text{eff}}^2 - \sin^2 \theta)^{1/2}$, where D is the diameter of the PS microspheres, n_{eff} is the effective refractive

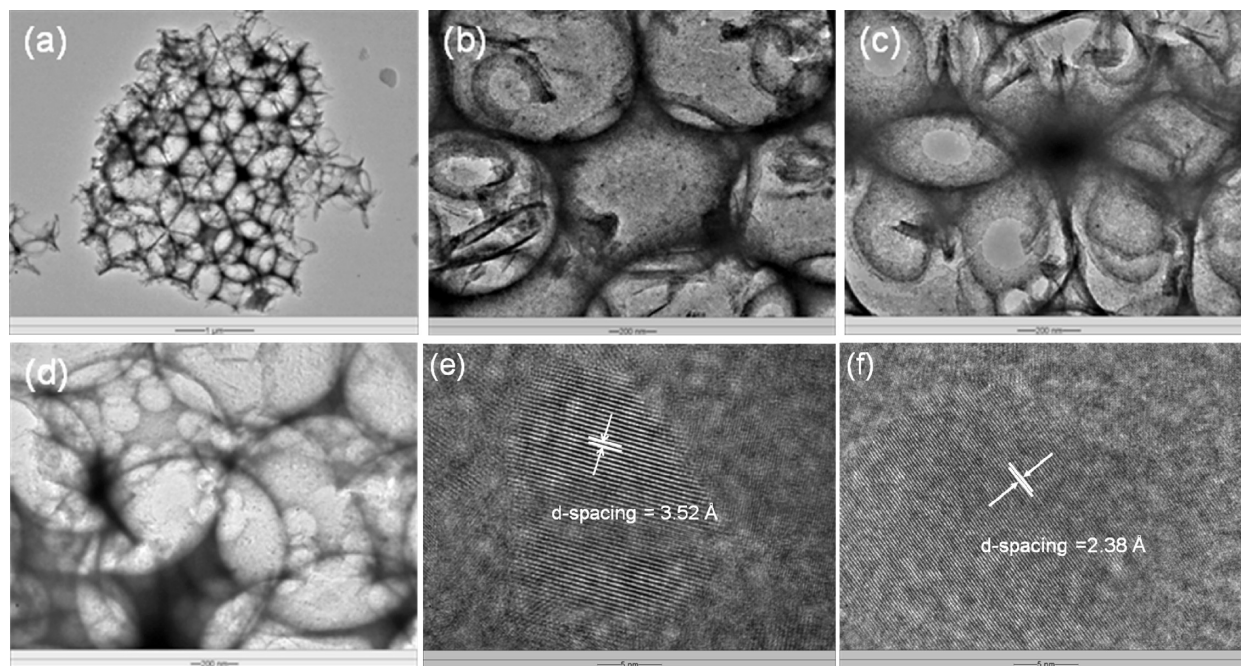


Figure 4. FETEM images of TiO_2 binary inverse opals with different porous structures. The number ratios of small to large spheres are (a–d) 2, 2, 4, and 8. (e, f) High-resolution TEM images showing the TiO_2 lattice.

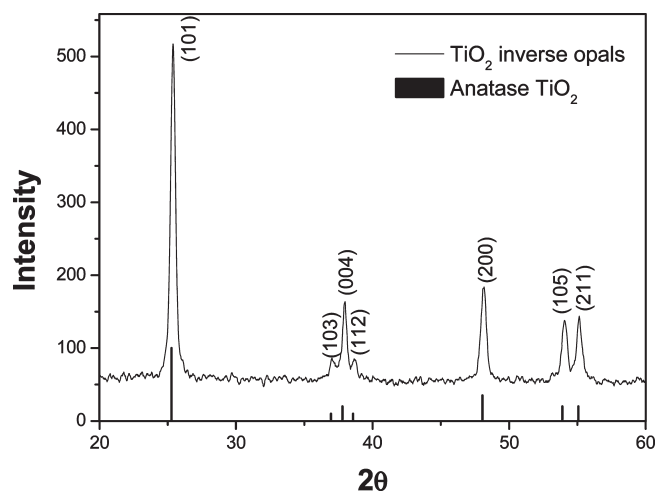


Figure 5. XRD pattern of the 3DOM TiO_2 binary inverse opals.

index, and θ is the angle between the incident and the reflective surface. In the calculation, a large sphere volume fraction of 0.74 for the fcc crystal lattice was assumed. The effective refractive indices of the PS bCCs and TiO_2 binary inverse opals were calculated using refractive indices of 1.59 for PS, 2.2 for anatase TiO_2 , and 1 for air. The measured reflectance peak wavelengths of PS bCCs agree reasonably well with the calculated peak wavelengths when taking into account experimental error. For TiO_2 binary inverse opals, however, the measured peak wavelengths deviate from the calculated reflectance spectra with a blue shift of ~ 200 nm. This blue shift can be attributed to the following two reasons. First, the TiO_2 inverse opals contracted when the samples were calcinated to remove the PS bCC template. As observed in the FESEM images, an $\sim 33\%$ contraction occurred by using this method. The other reason is that the theoretical

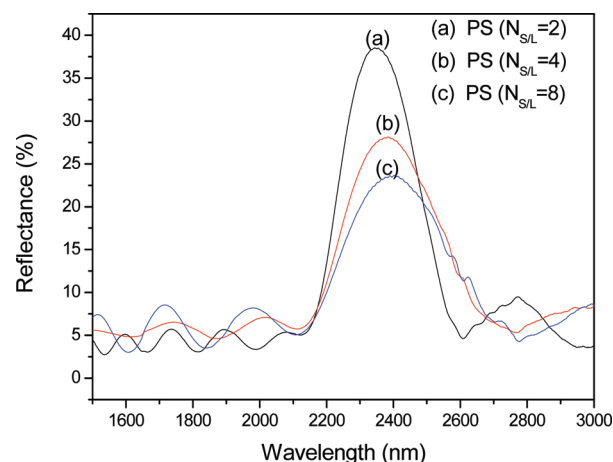


Figure 6. Reflectance spectra of PS bCCs fabricated with 170 and 1000 nm PS microspheres with number ratios of small to large microspheres of 2, 4, and 8, respectively.

maximum filling fraction of this geometry cannot be reached in the present study. The smaller filling ratio may cause a decreased effective refractive index of the 3DOM structures, leading to a blue shift of the pseudostop band peak wavelengths.

TiO_2 inverse opals have found applications in hydrogen fuel generation from water,^{37,38} photovoltaic cells,^{20,35,39} and photocatalysis for environmental remediation.^{40,41} One of the most intriguing properties of such periodic photonic structures of TiO_2 is their superior photocatalytic activity enabled by high surface/volume fractions and interconnected pores. In this work, the photocatalytic degradation of BA using TiO_2 inverse opals under UV light irradiation was investigated. TiO_2 nanoparticles prepared at the same sintering temperature as that of 3DOM TiO_2 were used as the reference. As shown in Figure 8, 3DOM

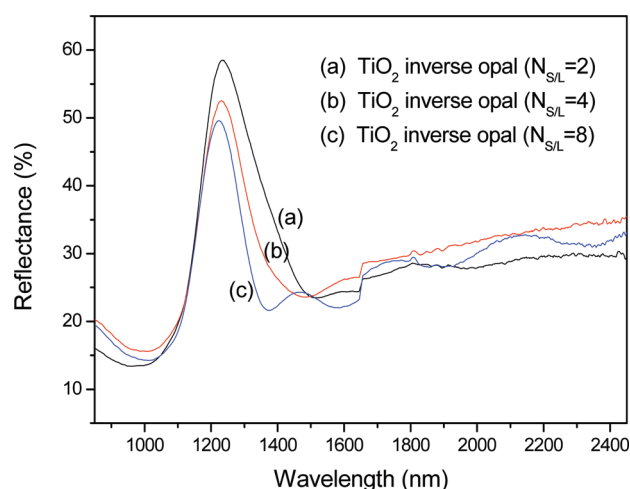


Figure 7. Reflectance spectra of the TiO_2 binary inverse opals fabricated by using PS bCC templates with number ratios of small to large microspheres of 2, 4, and 8, respectively.

Table 2. Calculated and Measured Stop Band Wavelengths

sample	assumed VF	assumed VF	calculated peak wavelength/nm	measured peak wavelength/nm
	of large sphere in sample	of small sphere in sample		
PS bCCs (2)	0.74	0.0104	2393	2342
PS bCCs (4)	0.74	0.0208	2401	2384
PS bCCs (8)	0.74	0.0416	2419	2402
In- TiO_2 (2)	0.74	0.0104	1488	1222
In- TiO_2 (4)	0.74	0.0208	1474	1230
In- TiO_2 (8)	0.74	0.0416	1445	1234

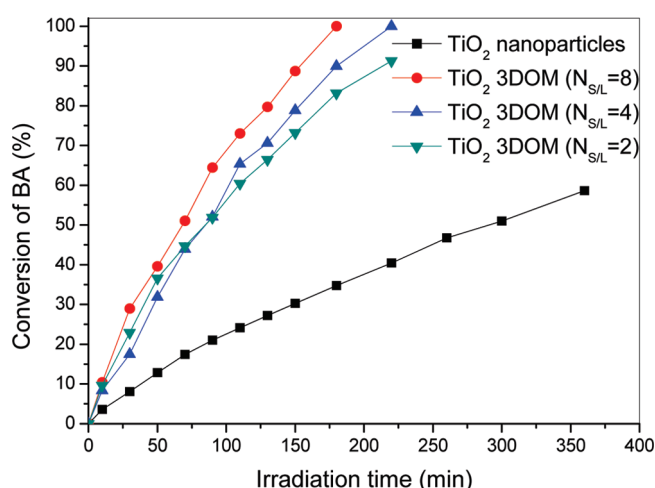


Figure 8. Photodegradation of BA using 3DOM TiO_2 and TiO_2 nanoparticles.

TiO_2 samples exhibit much higher activities than do the TiO_2 nanoparticles. In addition, the activity of 3DOM TiO_2 increases with the porosity of the binary inverse opals. The enhanced photocatalytic activity of the 3DOM TiO_2 structures can be mainly attributed to the increased specific surface of 3DOM

TiO_2 . The TiO_2 binary inverse opals have a larger specific surface (52 , 54 , and $57 \text{ m}^2/\text{g}$ for the TiO_2 binary inverse opals fabricated by using PS bCC templates with number ratios of small to large microspheres of 2, 4 and 8, respectively) than do the TiO_2 nanoparticles ($39 \text{ m}^2/\text{g}$) (Table S1, Supporting Information), which allows improved BA adsorption on the surface of TiO_2 and enhanced photocatalytic activity. In addition, the incorporation of 3DOM structure in TiO_2 photocatalysts may also improve the absorption of light because of the enhanced light scattering within the catalysts, resulting in enhanced photocatalytic activities.^{16,18,42} The 3DOM TiO_2 catalysts are very stable during the reaction, and the inverse opal structures can be retained even after about 4 h of irradiation (Figure S1, Supporting Information).

CONCLUSIONS

A sandwich-vacuum method was developed to fabricate large-area TiO_2 binary inverse opals with open pores and no overlayers in large domains. Using this method, we prepared 3DOM anatase TiO_2 with relatively uniform and ordered structures. The success of this method can be attributed to the use of a trifluoroacetic acid-modified precursor and the application of the sandwich-vacuum infiltration technique. Optical measurements of the PS bCCs and TiO_2 binary inverse opals indicate that the peak positions of the pseudostop bands were in agreement with the theoretical values. In addition, the 3DOM TiO_2 structures showed enhanced activity for BA photodegradation as a result of the increased path length of light within the catalysts and the large specific surface areas. This method is very reliable in fabricating TiO_2 inverse opals of high quality without using complicated apparatuses and procedures. The ease, reliability, and versatility of this method may provide an alternative to the fabrication of high-quality metal oxide inverse opals.

ASSOCIATED CONTENT

S Supporting Information. BET data of the samples. FES-EM and FETEM images of TiO_2 3DOM after photocatalytic reaction. This material is available free of charge via the Internet at <http://pubs.acs.org>.

AUTHOR INFORMATION

Corresponding Author

*Tel: (65)65164727. Fax: (65) 67791936. E-mail: chezxs@nus.edu.sg

ACKNOWLEDGMENT

This work was finally supported by the Environment and Water Industry Development Council (EWI) of Singapore (project number MEWR 651/06/161). The Taishan Scholars Programme of Shandong Province is acknowledged.

REFERENCES

- (1) Arsenault, A. C.; Clark, T. J.; von Freymann, G.; Cademartiri, L.; Sapienza, R.; Bertolotti, J.; Vekris, E.; Wong, S.; Kitaev, V.; Mannes, I.; Wang, R. Z.; John, S.; Wiersma, D.; Ozin, G. A. *Nat. Mater.* **2006**, *5*, 179–184.
- (2) Blanco, A.; Chomski, E.; Grabtchak, S.; Ibisate, M.; John, S.; Leonard, S. W.; Lopez, C.; Meseguer, F.; Miguez, H.; Mondia, J. P.; Ozin, G. A.; Toader, O.; van Driel, H. M. *Nature* **2000**, *405*, 437–440.
- (3) Rinne, S. A.; Garcia-Santamaria, F.; Braun, P. V. *Nat. Photon.* **2008**, *2*, 52–56.

- (4) Chen, J. I. L.; von Freymann, G.; Choi, S. Y.; Kitaev, V.; Ozin, G. A. *J. Mater. Chem.* **2008**, *18*, 369–373.
- (5) Lee, K.; Asher, S. A. *J. Am. Chem. Soc.* **2000**, *122*, 9534–9537.
- (6) Lee, Y.-J.; Pruzinsky, S. A.; Braun, P. V. *Langmuir* **2004**, *20*, 3096–3106.
- (7) Schroden, R. C.; Al-Daous, M.; Stein, A. *Chem. Mater.* **2001**, *13*, 2945–2950.
- (8) Yang, Y.; Yan, H.; Fu, Z.; Yang, B.; Xia, L.; Xu, Y.; Zuo, J.; Li, F. *J. Phys. Chem. B* **2005**, *110*, 846–852.
- (9) Ren, M.; Ravikrishna, R.; Valsaraj, K. T. *Environ. Sci. Technol.* **2006**, *40*, 7029–7033.
- (10) Holland, B. T.; Blanford, C. F.; Stein, A. *Science* **1998**, *281*, 538–540.
- (11) Guan, G.; Zapf, R.; Kolb, G.; Hessel, V.; Löwe, H.; Ye, J.; Zentel, R. *Int. J. Hydrogen Energy* **2008**, *33*, 797–801.
- (12) Velev, O. D.; Lenhoff, A. M. *Curr. Opin. Colloid Interface Sci.* **2000**, *5*, 56–63.
- (13) Xia, Y. N.; Gates, B.; Yin, Y. D.; Lu, Y. *Adv. Mater.* **2000**, *12*, 693–713.
- (14) Zhao, X. S.; Su, F.; Yan, Q.; Guo, W.; Bao, X. Y.; Lv, L.; Zhou, Z. *J. Mater. Chem.* **2006**, *16*, 637–648.
- (15) Stein, A.; Li, F.; Denny, N. R. *Chem. Mater.* **2007**, *20*, 649–666.
- (16) Chen, X.; Li, Z.; Ye, J.; Zou, Z. *Chem. Mater.* **2010**, *22*, 3583–3585.
- (17) Vekris, E.; Ozin, G.; Kitaev, V. *Adv. Mater.* **2006**, *18*, 2481–2485.
- (18) Chen, J.; von Freymann, G.; Choi, S.; Kitaev, V.; Ozin, G. *Adv. Mater.* **2006**, *18*, 1915–1919.
- (19) Chen, J. I. L.; von Freymann, G.; Kitaev, V.; Ozin, G. A. *J. Am. Chem. Soc.* **2007**, *129*, 1196–1202.
- (20) Nishimura, S.; Abrams, N.; Lewis, B. A.; Halaoui, L. I.; Mallouk, T. E.; Benkstein, K. D.; van de Lagemaat, J.; Frank, A. J. *J. Am. Chem. Soc.* **2003**, *125*, 6306–6310.
- (21) Halaoui, L. I.; Abrams, N. M.; Mallouk, T. E. *J. Phys. Chem. B* **2005**, *109*, 6334–6342.
- (22) Somani, P. R.; Dionigi, C.; Murgia, M.; Palles, D.; Nozar, P.; Ruani, G. *Sol. Energy Mater. Sol. Cells* **2005**, *87*, 513–519.
- (23) Huisman, C. L.; Schoonman, J.; Goossens, A. *Sol. Energy Mater. Sol. Cells* **2005**, *85*, 115–124.
- (24) Rodriguez, I.; Ramiro-Manzano, F.; Atienzar, P.; Martinez, J. M.; Meseguer, F.; Garcia, H.; Corma, A. *J. Mater. Chem.* **2007**, *17*, 3205–3209.
- (25) Wijnhoven, J. E.; nbsp, G.; J.; Vos, W. L. *Science* **1998**, *281*, 802–804.
- (26) Galusha, J. W.; Tsung, C.-K.; Stucky, G. D.; Bartl, M. H. *Chem. Mater.* **2008**, *20*, 4925–4930.
- (27) Wijnhoven, J.; Bechger, L.; Vos, W. L. *Chem. Mater.* **2001**, *13*, 4486–4499.
- (28) Ni, P.; Dong, P.; Cheng, B.; Li, X.; Zhang, D. *Adv. Mater.* **2001**, *13*, 437–441.
- (29) Stein, A.; Schroden, R. C. *Curr. Opin. Solid State Mater. Sci.* **2001**, *5*, 553–564.
- (30) Bartl, M. H.; Boettcher, S. W.; Hu, E. L.; Stucky, G. D. *J. Am. Chem. Soc.* **2004**, *126*, 10826–10827.
- (31) Bartl, M. H.; Boettcher, S. W.; Frindell, K. L.; Stucky, G. D. *Acc. Chem. Res.* **2005**, *38*, 263–271.
- (32) Boettcher, S. W.; Bartl, M. H.; Hu, J. G.; Stucky, G. D. *J. Am. Chem. Soc.* **2005**, *127*, 9721–9730.
- (33) Shim, S.-E.; Cha, Y.-J.; Byun, J.-M.; Choe, S. J. *Appl. Polym. Sci.* **1999**, *71*, 2259–2269.
- (34) Wang, L.; Wan, Y.; Li, Y.; Cai, Z.; Li, H.-L.; Zhao, X. S.; Li, Q. *Langmuir* **2009**, *25*, 6753–6759.
- (35) Kwak, E. S.; Lee, W.; Park, N. G.; Kim, J.; Lee, H. *Adv. Funct. Mater.* **2009**, *19*, 1093–1099.
- (36) Reculosa, S.; Ravaine, S. *Chem. Mater.* **2003**, *15*, 598–605.
- (37) Bard, A. J.; Fox, M. A. *Acc. Chem. Res.* **1995**, *28*, 141–145.
- (38) Liu, J.; Liu, G.; Li, M.; Shen, W.; Liu, Z.; Wang, J.; Zhao, J.; Jiang, L.; Song, Y. *Energy Environ. Sci.* **2010**, *3*, 1503–1506.
- (39) Lee, S.-H. A.; Abrams, N. M.; Hoertz, P. G.; Barber, G. D.; Halaoui, L. I.; Mallouk, T. E. *J. Phys. Chem. B* **2008**, *112*, 14415–14421.
- (40) Fox, M. A.; Dulay, M. T. *Chem. Rev.* **1993**, *93*, 341–357.
- (41) Chen, J. I. L.; Loso, E.; Ebrahim, N.; Ozin, G. A. *J. Am. Chem. Soc.* **2008**, *130*, 5420–5421.
- (42) Hore, S.; Nitz, P.; Vetter, C.; Prahl, C.; Niggemann, M.; Kern, R. *Chem. Commun.* **2005**, 2011–2013.